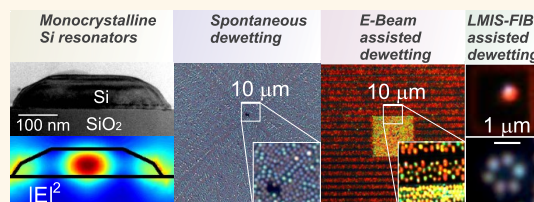


Wafer Scale Formation of Monocrystalline Silicon-Based Mie Resonators *via* Silicon-on-Insulator Dewetting

Marco Abbarchi,^{*,†} Meher Naffouti,^{†,II} Benjamin Vial,[‡] Abdelmalek Benkouider,[†] Laurent Lermusiaux,[§] Luc Favre,[†] Antoine Ronda,[†] Sébastien Bidault,[§] Isabelle Berbezier,[†] and Nicolas Bonod^{*,‡}

[†]CNRS, Aix-Marseille Université, Centrale Marseille, IM2NP, UMR 7334, Campus de St. Jérôme, 13397 Marseille, France, [‡]CNRS, Aix-Marseille Université, Centrale Marseille, Institut Fresnel, UMR 7249, Campus de St. Jérôme, 13397 Marseille, France, [§]Institut Langevin, ESPCI ParisTech, CNRS UMR 7587, Paris, France, and ^{II}Laboratoire de Micro-optoélectronique et Nanostructures, Faculté des Sciences de Monastir, 5019 Monastir, Tunisia

ABSTRACT Subwavelength-sized dielectric Mie resonators have recently emerged as a promising photonic platform, as they combine the advantages of dielectric microstructures and metallic nanoparticles supporting surface plasmon polaritons. Here, we report the capabilities of a dewetting-based process, independent of the sample size, to fabricate Si-based resonators over large scales starting from commercial silicon-on-insulator (SOI) substrates. Spontaneous dewetting is shown to allow the production of monocrystalline Mie-resonators that feature two resonant modes in the visible spectrum, as observed in confocal scattering spectroscopy. Homogeneous scattering responses and improved spatial ordering of the Si-based resonators are observed when dewetting is assisted by electron beam lithography. Finally, exploiting different thermal agglomeration regimes, we highlight the versatility of this technique, which, when assisted by focused ion beam nanopatterning, produces monocrystalline nanocrystals with ad hoc size, position, and organization in complex multimers.



KEYWORDS: Mie resonators · thin film dewetting · all-dielectric nanophotonics · silicon nanoparticles

Dielectric Mie resonators (MRs) are valuable alternatives to plasmonic nanoparticles to manipulate light-matter interactions.^{1–12} Compared with their metallic counterparts, dielectric MRs, whose refractive index is larger than $n = 2.5$, feature the unique ability to exhibit both electric and magnetic modes that completely redistribute scattering and emission patterns.^{13–23} This novel class of resonant scatterers is very promising for several reasons: (i) their absorption losses are very weak in the optical and near-infrared range of frequencies; (ii) their scattering properties, resulting from the interference between magnetic and electric modes, can be tuned by modifying the particle shape and/or refractive index; and (iii) they are compatible with silicon-based nanofabrication technologies. Different approaches have been followed over the last two years to fabricate silicon submicrometric particles such as laser ablation^{4,5,12} and electron

beam lithography associated with reactive ion etching (EBL)^{16,18,24} or nanoimprint processes¹⁹ in the visible range, as well as chemical vapor deposition⁸ and colloidal synthesis⁹ at near-infrared wavelengths. However, the successful implementation of MRs in silicon devices at visible frequencies still requires a cost-effective and reliable technique for producing high quality crystalline particles that can be coupled with silicon-on-insulator (SOI) substrates.

Here, we follow a different approach that allows to produce monocrystalline islands over full wafers and to organize them in complex patterns. This technique is based on the dewetting of ultrathin crystalline silicon films that leads to high quality monocrystalline silicon nanodroplets. These sub-micrometric sized particles exhibit a truncated pyramidal shape characterized by the low-energy facets ((113), (111) and (001)) of the crystalline silicon phase. This study reports the first optical characterization of

* Address correspondence to
marco.abbarchi@im2np.fr,
nicolas.bonod@Fresnel.fr.

Received for review May 15, 2014
and accepted November 3, 2014.

Published online November 03, 2014
10.1021/nn505632b

© 2014 American Chemical Society

Mie resonators obtained *via* a dewetting approach. Importantly, this self-assembling dewetting approach requires only one fabrication step, *i.e.*, annealing under a high vacuum, to fabricate Mie resonators over large scales. The strength of this approach relies on a fast process that does not depend on the size of the sample, but only on the dewetting speed.^{25–31}

RESULTS AND DISCUSSION

Morphological and Optical Characterization of Single Mie Resonators. Dewetting at liquid/solid and solid/solid interfaces is an ubiquitous phenomenon in nature^{32,33} and has a tremendous impact on the self-assembly of micro- and nanostructures.^{34,35} The protocol followed in this work is based on the instability of ultrathin Si films (typically less than 30 nm) on a SiO₂/Si substrate when annealed at high temperatures (750–880 °C) in a high-vacuum chamber (10^{–8}–10^{–10} Torr).^{25–29,36–38} The planar crystalline silicon film evolves first with the formation of holes which then expand over the SiO₂ layer. During the lateral expansion of the holes, the thin-film breaks up to form isolated Si nanocrystals which finally evolve toward truncated pyramidal nanocrystals exhibiting a faceted shape with the onset of the low-energy facets: (111), (113) and (001)²⁹ (see also Figure S1 of the Supporting Information). A typical transmission electron microscopy (TEM) image of a dewetted MR is given in Figure 1a. A pseudohexagonal spot-pattern in the fast Fourier transform (FFT) of the TEM image (inset) attests the equilibrium shape and monocrystalline nature of the nanostructure. This morphology is representative of the balance between the wetting interfacial energy between Si and SiO₂ and the anisotropic surface energy.

We now aim at measuring the typical scattering spectra of truncated pyramidal-shaped silicon nanocrystals in order to evaluate whether the dewetting process is compatible with visible frequency resonances. For that purpose, we investigate a partially dewetted sample that locally exhibits isolated nanocrystals with separation distances exceeding several microns for which electromagnetic coupling between neighboring MRs can be neglected. Partial dewetting has two advantages for spectroscopic studies of individual MRs: (i) large interparticle distances that are compatible with confocal microscopy for the analysis of individual MRs; (ii) a wide size distribution of the nanocrystals that allows a systematic study.

Figure 1b (left panel) shows a reflection darkfield (DF) image of MRs obtained by annealing at 850 °C, for 25 min, a SOI substrate featuring a 11 nm thick silicon layer on a 145 nm SiO₂ layer. Comparison of the same isolated Si crystals in darkfield and atomic force microscopies (AFM) on Figure 1b indicates that resonators with different shapes and sizes exhibit different resonance frequencies. The morphological characterization of 20 scatterers using AFM shows the formation

of islands with an average base size L ranging between ~250 and ~400 nm (see also Figure S3 in the Supporting Information) and with heights h ranging between ~50 and ~85 nm. The vertical aspect ratio $\eta = h/L$ is close to ≈ 0.2 and stays constant in the investigated range of particle sizes. This morphological analysis was only performed on scatterers exhibiting resonances in the visible spectrum but the sample also features larger islands that should correspond to near-infrared responses (additional informations on the morphology of the dewetted islands can be found in Figure S1 and Figure S3 of the Supporting Information).

The scattering spectra of isolated resonators are measured using a darkfield microscope fiber-coupled to an imaging spectrometer (see also Figure S2 in the Supporting Information). The 50 μm wide multimode fiber allows the spatial selection of individual MRs with a $\sim 1 \mu\text{m}$ lateral resolution. Figure 1d (left panel) provides typical measured spectra for Si resonators with varying in-plane sizes L and heights h estimated in AFM. L is the average in-plane size $(L_m + L_M)/2$ with L_m and L_M the small and large lengths.

We observe that all the spectra are characterized by two main broad peaks (A and B) that are the signature of the resonant excitation of two different modes in the Si crystals. Both peaks are red-shifted when h and L are increased from 53 to 72 nm and 250 to 400 nm, respectively. Moreover, it can be observed that the relative height of the two resonant modes A and B is inverted when increasing the MR size. Spectroscopic measurements were performed on the 20 resonators studied by AFM and the evolution of the resonance frequencies, for the two main modes with respect to the particle size, is given in the Supporting Information (Figure S3). We observe that all studied Si crystals, even with varying in-plane shape anisotropies, feature two main resonances that red-shift for increased particle sizes. This is the expected behavior for resonators governed by radiative damping that increases for larger particles.³⁹

In order to provide further insight in the two observed resonances, we perform numerical simulations using a finite element method that is compatible with the faceted shape of the monocrystalline resonators. The shape of the resonators as well as the substrate are expected to play an important role,⁴⁰ and we take into account in the finite element model the major geometrical parameters estimated by AFM (L and h reported in Figure 1c) and the different layers of the SOI substrate. To take into account the excitation geometry offered by reflection dark field microscopy (see Figure S2), we compute the scattered electromagnetic field in air (Figure 1d right panel) when the MR is illuminated by a plane wave with an angle of incidence of 70 degrees for the 6 resonators considered in Figure 1d (left panel). The numerical

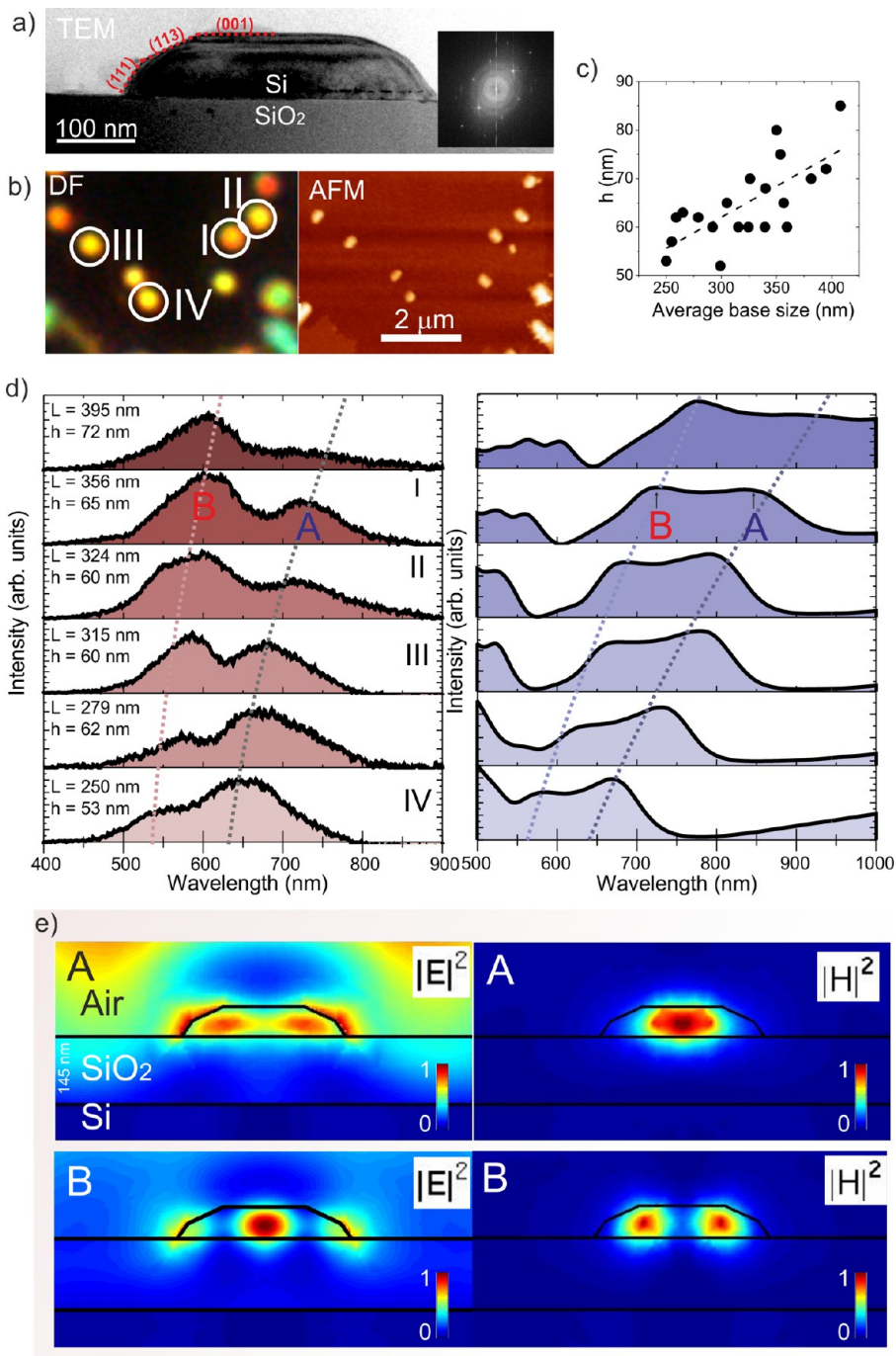


Figure 1. Morphological and optical characterization of single Mie resonators. (a) TEM image of a single silicon Mie resonator. The crystallographic facets (111), (113) and (001) are highlighted. The inset provides the fast Fourier transform of the image, demonstrating the crystalline nature of the particle. (b) Darkfield (DF) optical microscope image (100 \times magnification objective lens) of a partially dewetted sample (left panel) and corresponding atomic force microscope (AFM) topography (right panel). White circles surround 4 resonators whose DF spectra are shown in (d). (c) MR height as a function of the corresponding base size as measured by atomic force microscopy (AFM). The dashed line is a linear fit to the data. (d) Left panel: DF backscattering spectra of six MRs with increasing sizes from bottom to top panel (height h and base size L are given for each spectrum). Right panel: numerical simulations of the scattering spectra obtained with the finite element method considering the 6 MRs shown in the left panel. The dashed lines in the two panels are guides to the eyes. (e) Reconstruction of the electric $|E|^2$ and magnetic $|H|^2$ field intensity in the vicinity of the resonator I in (c) ($L = 356$ nm and $h = 65$ nm).

simulations confirm the excitation of two modes in the resonators with frequencies that are red-shifted for increased particle sizes. Importantly, these calculations also reproduce the inversion of the relative height of

both peaks when increasing the particle size as well as the $A-B$ mode-splitting. Let us stress that the numerical simulations catch the main features and evolutions observed in experiments even if differences

are observed with the experimental data (*i.e.*, smaller broadening, shorter resonant wavelengths and steeper slope with increasing size) that can be attributed mainly to in-plane shape anisotropy (see Figure S3a of the Supporting Information).

We now address the physical origin of the *A* and *B* resonances. Their different nature is highlighted by computing the electric and magnetic field intensities at the two resonant frequencies in the vicinity of the resonator on Figure 1e. The calculations are performed for the resonator denoted *l* with $L = 356$ nm and $h = 65$ nm. The norm of the electric field $|E|^2$ is displayed when the resonator is illuminated by a plane wave with an angle of incidence of 70 degrees. We observe very different field distributions since the *B* resonance corresponds to the formation of a single spot in the middle of the cavity while the *A* mode provides two spots near the edge of the Si island and a strong field intensity outside the resonator. Please note that the field maps are symmetric because of an averaging of the excitation (see Methods) in order to take into account the symmetry of the incident beam. As shown on Figure 1e, the two $|E|^2$ spots of mode *A* lead to an enhancement of the magnetic field in the center of the resonator. These maps indicate that mode *A* is dominated by an in-plane dipolar magnetic mode.⁴⁰ Symmetrically, the electric field enhancement in the center of the cavity in mode *B* is related to two spots of the magnetic field, indicating an electric dipolar resonance. These maps evidence the fact that the two peaks are mostly linked to the excitation of the first two Mie dipolar modes inside the Si resonators.

Spectroscopic measurements correlated to a systematic morphological analysis and full-field simulations on single Si-nanocrystals demonstrate that the dewetting technique is able to produce Mie resonators exhibiting well-defined magnetic and electric modes in the visible spectrum.

Spontaneous and Assisted Dewetting. Spontaneous dewetting of silicon thin-films is either triggered by local defectivity (extended defects and surface impurities) or, in the case investigated here of SOI substrates where defectivity is very low, by O₂ vacancies associated with a dry thermal oxidation mechanism.^{27,28,31,38} The spatial distribution of the islands during the film retraction is controlled by a Rayleigh-like instability^{37,41} which is characterized first, by the formation of holes and the consequent retraction of the 2D thin film and formation of a rim. In optimal conditions, the dewetting front breaks while forming elongated structures (*fingers*) which, in turn, break to form islands aligned along the crystallographic axes $\langle 100 \rangle$ and $\langle 010 \rangle$. The nontrivial interplay of these factors, together with the experimental conditions (SOI thickness, annealing temperature and time), leads to very different types of self-ordering or random

organization of the nanocrystals. We observe the typical Rayleigh-like features in Figure 2a (top panel) where relatively low annealing temperatures (780 °C) are used. The bottom panel of Figure 2a shows a different sample (with the same composition than in top panel) where a complete transition from planar film to 3D islands is observed for the SOI substrate over a large surface (90 μm in the figure). Larger scales are reported in the Supporting Information (Figure S4a and Figure S5) to evidence the efficiency of the process at centimeter scales for different samples. Remarkably, ordered islands can be created with this technique over the full sample in a few hours, independently on the size of the sample. Moreover, the number of steps required to achieve these results is significantly reduced with respect to any conventional lithographic technique.

When higher annealing temperatures are used, the organization of the islands on a regular pattern is progressively lost. Figure 2b and Figure S4b show, that at higher temperatures (840 °C for Figure 2b, 880 °C in Figure S4b), the dewetting front switches from squares to circles, while the ordering of the Si-islands is partially or completely lost. We interpret this behavior as an effect related to local strain accumulation and relaxation promoted by the fast dewetting dynamics, SiO₂ mixing, and to a progressively increased promotion of SiC centers. All the effects drastically modify the surface atom diffusion leading to anomalous dewetting behaviors.³⁷ This is quite evident in Figure 2c that displays the result of dewetting with a SOI substrate previously contaminated by chemical processing during the fabrication steps of electronic lithography and annealed at high temperature (850 °C).

These examples show the versatility of the dewetting approach to control the ordering/disordering degree of nanostructured silicon by simply tuning the annealing temperature. This control can have major applications in photonics where ordered arrays with homogeneously distributed objects are required for promoting a narrow working bandwidth while a larger dispersion of size and disordering is expected to widen the working bandwidth and is very interesting to manipulate light diffusion in complex scattering media.^{42–46}

Finally, we observe that a change of the thickness of the underlying SiO₂, through a Fabry-Pérot like effect,⁴⁰ has a dramatic influence on the scattering properties as evidenced when comparing Figure 2b and Figure 2c where, in spite of a small change in the top silicon thickness (12 nm in Figure 2b and 11 nm in Figure 2c), a completely different light scattering is observed.

To further control the structural properties of MRs, we propose to combine the self-assembling approach of the dewetting technique with a top-down pre-patterning. In practice, since dewetting proceeds *via* surface atom diffusion, the main crystallographic axes

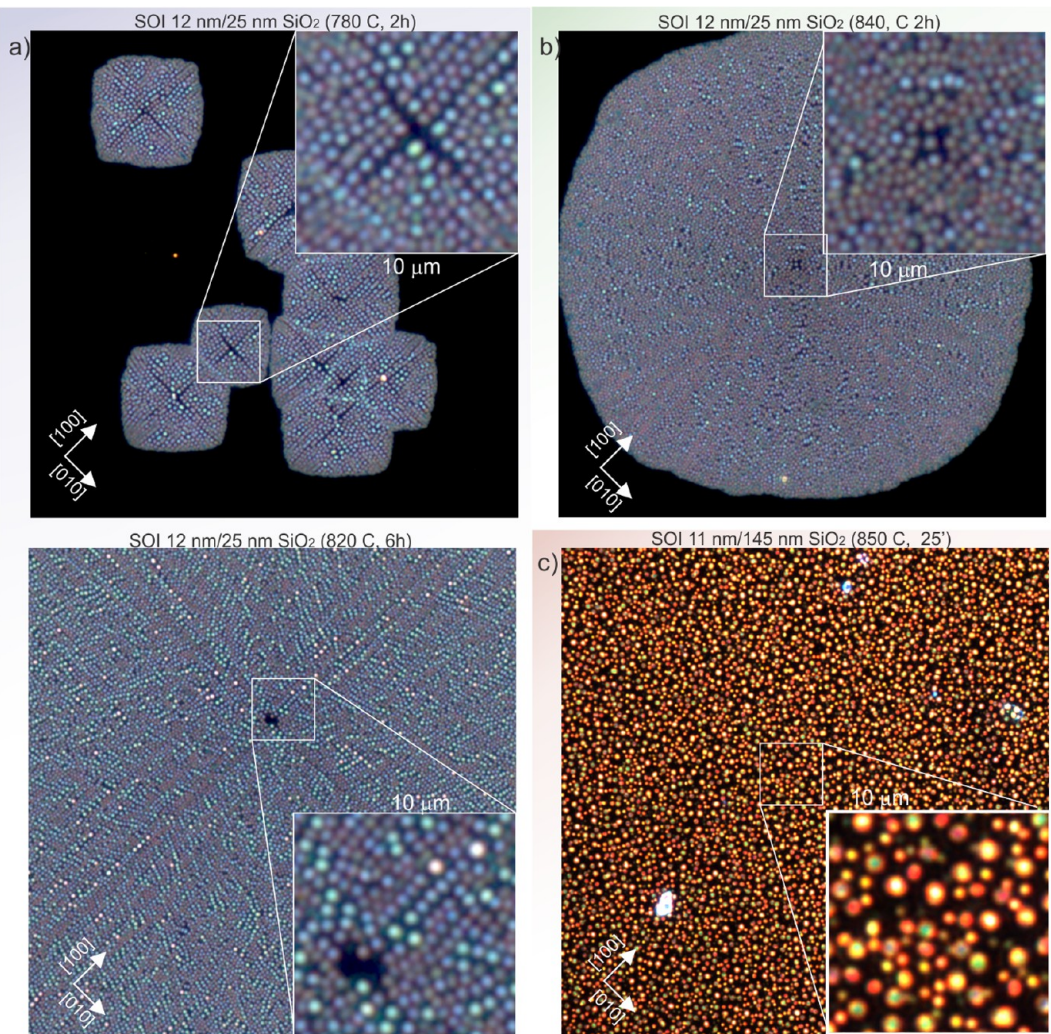


Figure 2. Spontaneous dewetting. Dark-field microscope images ($100\times$) of spontaneously dewetted SOI substrates. The highlighted $10\ \mu\text{m} \times 10\ \mu\text{m}$ areas are enlarged in the insets. The crystallographic axes are shown. (a) SOI 12 nm Si film on 25 nm of SiO_2 annealed at $T = 780\ ^\circ\text{C}$ for 2 h (top panel) and 6 h (bottom panel). (b) Same as (a) top panel but for higher temperature $T = 840\ ^\circ\text{C}$ (see also Figure S4b in the Supporting Information for the case of dewetting at $880\ ^\circ\text{C}$). (c) SOI 11 nm of Si on 145 nm of SiO_2 annealed at $T = 850\ ^\circ\text{C}$ for 25'. The sample was contaminated by a e-beam etching lithographic process (in a different area) before annealing (see also Figure 3 and Figure S6 in the Supporting Information for similar DF images in different areas and similar samples).

are the favored directions and introducing patterns that are diagonal or parallel to these directions leads to important changes in the final result.^{30,41} In fact, differently oriented dewetting fronts show a different instability evolution: the $\langle 110 \rangle$ straight fronts are stable and typically evolve by retraction while $\langle 100 \rangle$ fronts are unstable and evolve by fingers formation and dewetting.³⁷

We take advantage of these properties by patterning the SOI substrates by electron beam lithography associated with reactive ion etching (EBL) before annealing the samples. In Figure 3 and Figure S6, the upper layer of the SOI substrates is etched with parallel grooves of different widths, aligned with the $[100]$ crystallographic direction (see region A in Figure 3 and Figure S6). The width of the etched grooves decreases from bottom to top. By comparing zone A

with unetched zones (for example, region B in Figure 3), we observe a more homogeneous scattering between the etched grooves (typically in the red part of the spectrum for this resonator size range). This is a direct consequence of the higher ordering and size homogeneity allowed by the etching process.^{30,31} In the same etched pattern, a central region has been added with etched grooves separated by $1\ \mu\text{m}$ (see region C in Figure 3 and in Figure S6). The decrease of the distance between the grooves induces a decrease of the main size of the resonators leading to a significant shift of the spectral properties of the central zone. This result is very interesting since it reveals that the spectral features of Si-based devices can be controlled spatially over large scales without a precise etching of each individual resonators. Let us emphasize that this fabrication technique relies on a self-assembling approach

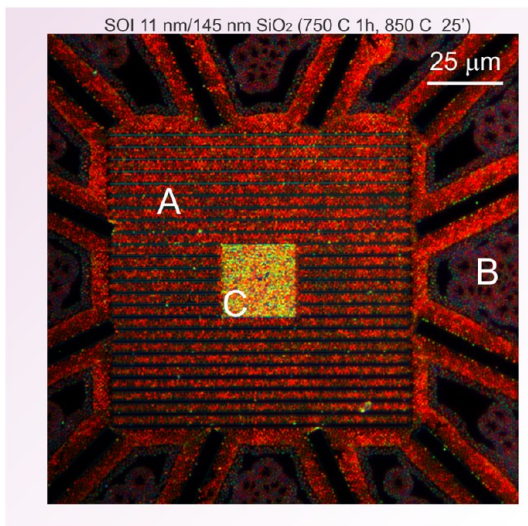


Figure 3. E-beam assisted dewetting. DF image (50 \times magnification) of a 11 nm Si film on a 145 nm SiO₂ layer (annealed at 750 °C for 1 h plus 25 min at 850 °C). The sample was prepatterned with parallel lines aligned with [100] by EBL before dewetting. The etched pattern has an interline spacing of 4 μ m in the external part while it is only 1 μ m in the central part.

and does not require the templating of individual scatterers like in standard lithographic techniques. Finally an ultimate control of the spectral properties of MRs can be obtained by etching additional grooves along the orthogonal [110] direction^{30,31} (see region C in Figure S6). Similar results were obtained on different samples (*i.e.*, different SOI thicknesses) confirming the validity of this approach (see for example Figure S6 where three repetitions of the same pattern are shown).

Position Control of Individual and Complex Assemblies of Mie Resonators. As discussed previously, spontaneous and assisted dewetting processes are fabrication methods adapted for large scale applications. To further demonstrate the flexibility of heterogeneous dewetting, we show that a precise positioning of individual and isolated MRs can be achieved by prepatternning the SOI samples using a liquid-metal ion alloy source-based focused ion beam (LMAIS-FIB) milling approach. For that purpose, we tune the dewetting speed in order to promote two different regimes of island formation:³⁶ (A) *formation of individual MRs* obtained with slow dewetting speed, *i.e.*, low annealing temperature, and (B) *formation of complex assemblies of MRs* obtained with fast dewetting, *i.e.*, higher temperature. We provide a quantitative study in analyzing the results obtained on samples etched by LMAIS-FIB in squared and circular patterns (thus limiting the available amount of dewettable material) that are dewetted at different temperatures (780 and 800 °C).

Isolated Mie Resonators. For small SOI domains (few μ m size) etched by LMAIS-FIB combined with a slow dewetting speed (annealing of 11 nm Si on 145 nm

SiO₂ at 780 °C for 2 h + deposition of 2 Ge monolayers), the dominant behavior is characterized by a growth of single islands.³⁶

The dewetting regime (A) is analyzed with respect to the presence or not of a hole milled at the center of the template. An example of etched pattern is shown in Figure 4a where a (3D) scheme is reported. The same schemes (2D) are also reported on the left panels of Figure 4d together with bright and dark field images obtained from the dewetted sample (respectively right and central panels in Figure 4d). The BF images display the denuded oxide as dark-blue and the nondewetted silicon in white color. In the DF images counterpart, the rim appears as red-orange color. The initial etched pattern is displayed in white dotted lines.

This analysis reveals that for this slow dewetting speed, the formation of individual MRs requires the presence of a central hole. Indeed, in the first case (without initial hole), the annealing step leads only to the enlargement of the etched grooves and in the second case (with initial hole), to the formation of an island at the center. In this latter case, the presence of a central hole acts as a deterministic nucleation center for the large central island.

A detailed analysis of the AFM measurements performed on the pattern with a hole is displayed in Figure 4b and in Figure 4c. The relevant features are summarized as follows: the island height is about 100 nm (Figure 4c top panel (i)), this value is remarkably larger with respect to that found for faster dewetting speed (*i.e.*, larger annealing temperature in the dewetting regime B) which showed 50–80 nm heights (see Figure 5 and comments). Besides, we also observe a second small island, of about \sim 10 nm in height (see Figure 4c bottom panel (iii)). This second island is not visible in either DF or BF images as it is too small to scatter light significantly. Finally, a small rim (characterized by AFM in Figure 4c central panel (ii)) is observed around the etched grooves and the central hole. If we compare the dewetting speeds V_{in} and V_{out} defined in panel (iii) of Figure 4b, we observe an asymmetric behavior ($V_{in} < V_{out}$). Remarkably, the typical distance of the largest island from the central hole milled by FIB is usually smaller than 500 nm. This fabrication method was tested under several geometrical configurations, on different parts of the sample and with different etching parameters (such as the etching depth) and the nucleation of a large central island was always associated with the presence of a central hole.

The statistics of the results obtained with circular patterns, associated or not with holes in the enclosed area, are shown in Figure 4e (square and diamond shapes with different orientations and sizes provide the same results and are not shown). For both cases, four different sizes are considered and characterized (diameter changing from 2.5 to 4 μ m in steps of

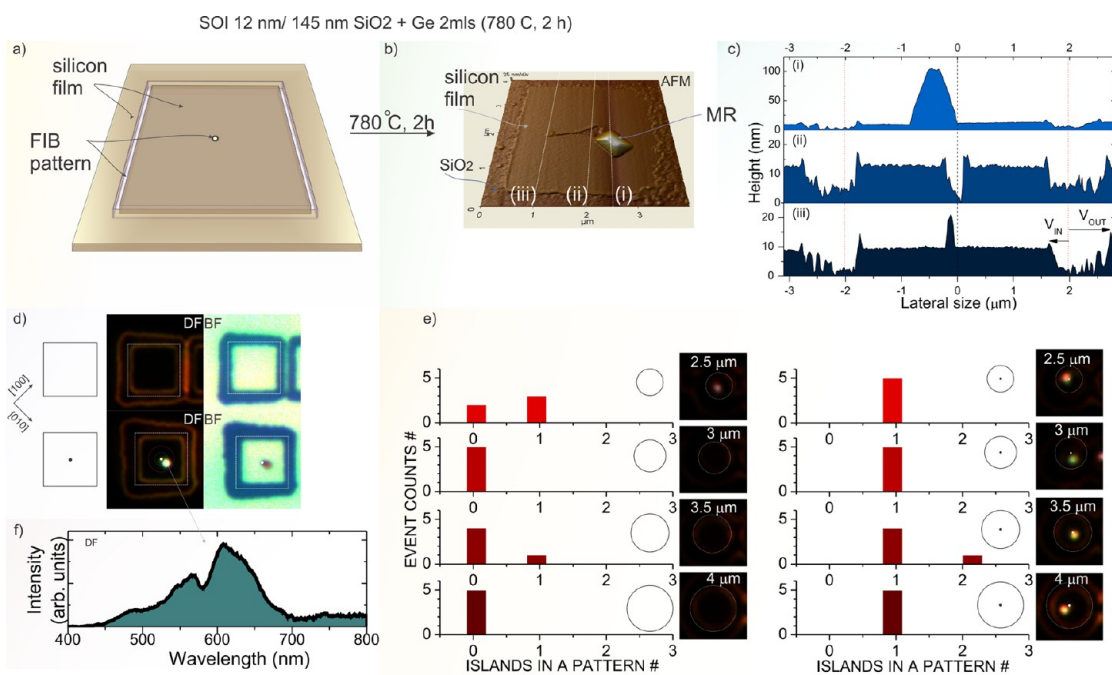


Figure 4. Position control of individual Mie resonators. (a) Scheme of the top crystalline Si-layer of a SOI substrate (12 nm Si on 145 nm SiO₂) milled by LMAIS-FIB in a square pattern with a hole at its center (hole diameter ~100 nm). (b) 3D AFM image of a partially dewetted pattern (4 μm square with a hole at the center after annealing for 2 h at 780°C and deposition of 2 Ge monolayers). In the figure are visible the Mie resonator nearby the (enlarged) central hole and a part of the nondewetted 2D silicon film (of about 3.5 μm in the lateral direction). White dotted lines (i), (ii), and (iii) are reported as AFM profiles in graph (c) respectively in the top, central and bottom panels. (c) Top panel (i): AFM profile of the MRs shown in (b). Central (ii) and bottom (iii) panels: details of the profile of the milled central hole and 1 μm on its left. A rim of about 5 nm in height and a very small island (h = 10 nm) are visible. The vertical dotted red lines indicate the initial position of the patterned template, while V_{in} and V_{out} shows the asymmetric dewetting speeds respectively toward the center and outside of the etched pattern. (d) Left row: sketch of the initial square template milled by LMAIS-FIB with and without a hole. The square size is 4 μm and the same pattern is overlapped on the other panels as white squares. Middle and right rows: 100× dark (DF) and bright field (BF) images of the MR shown in (b) and (c). The empty square does not lead to the formation of islands. In BF images, the remaining silicon appears in white while the underlying SiO₂ appears in dark blue. The slow dewetting speed leads to the formation of a Mie resonator only if a small pit is imprinted in the area. The single MR is clearly observable in both DF and BF images. (e) Statistics of the number of nucleated islands in 5 trials of circular patterns changing the diameter from 2.5 μm to 4 μm in step of 0.5 μm. The left panel shows the case of circles without a hole and the right panel with a hole. Milled template and corresponding DF image of the annealed sample are reported as insets for each case. (f) Dark field spectrum of the MR shown in (b), (c), and (d).

0.5 μm). For each diameter, five repetitions of the same pattern are produced. In the first case (without initial hole shown in Figure 4e left panel), the annealing leads to the formation of silicon resonators only for the smallest patterns (2.5 μm in diameter) with a poor control and poor spatial localization,³⁶ while for larger sizes (diameters larger than 3 μm), it does not lead to the formation of MRs in 14 structures out of 15 (93%). In the second case (with an initial hole at the center of the enclosed area; Figure 4e right panel), the dewetting leads to the deterministic formation of individual Si-resonators with a high reliability (95%).

Finally, this regime leads to the formation of single MRs featuring a resonant interaction with incident light as confirmed in Figure 4f displaying a typical dark-field spectrum. As in the case of spontaneously dewetted islands (see Figure 1), we observe two main peaks which are interpreted in the same framework of magnetic and electric dipolar resonances.

Complex Assemblies of Mie Resonators. Silicon metasurfaces and silicon nanoparticle oligomers have recently attracted a keen interest due to their ability to feature Fano anomalies.^{47,48} To promote the formation of assemblies of Mie resonators, the annealing temperature is raised to drive the dewetting instability to a different regime where many crystalline islands are formed simultaneously.³⁶

As for the previous regime, we investigate the effect of LMAIS-FIB patterning in terms of the presence or absence of additional features in the template. A SOI substrate (12 nm SOI on 25 nm SiO₂) is now annealed at 800 °C for 1 h. Examples of circles with or without a hole are investigated by AFM measurements (see Figure 5a). We observe that this novel dewetting regime leads to the formation of several islands in contrast to the previous case. The absence of the central hole typically leads to a relatively disordered behavior (large variation of number of dewetted MRs, low control of position and inhomogeneous size³⁶). A better

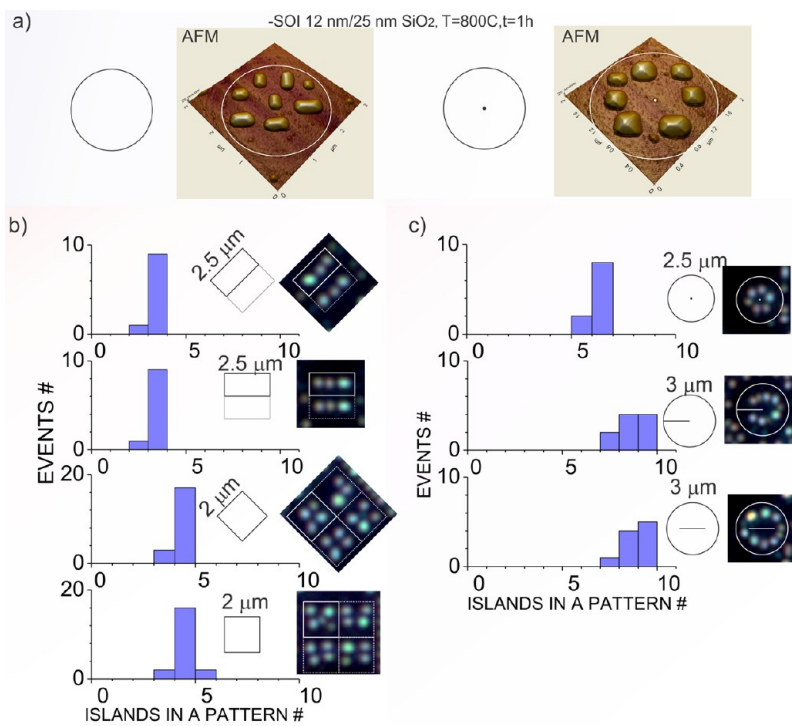


Figure 5. Controlled patterns of Mie resonator assemblies. (a) AFM images of dewetted circular patterns with and without a hole at the center. The diameter of the circle was $3\text{ }\mu\text{m}$ for the left panel and $2.5\text{ }\mu\text{m}$ for the right panel. The patterns are highlighted in white. The sample was a SOI 11 nm Si on 25 nm of SiO₂ annealed at $T = 800\text{ }^{\circ}\text{C}$ for 1 h. (b) Statistical distribution for MRs formed within a template for rectangles ($2.5\text{ }\mu\text{m} \times 1.25\text{ }\mu\text{m}$) and squares $2\text{ }\mu\text{m} \times 2\text{ }\mu\text{m}$ having different orientations. (c) Same as (b) for circular patterns with hole ($2.5\text{ }\mu\text{m}$ in diameter) and dashes ($3\text{ }\mu\text{m}$).

homogeneity and ordering is instead obtained when a hole is milled and, more generally, for smaller patterns (typical dimension $\leq 2.5\text{ }\mu\text{m}$): in Figure 5a right panel, the circular organization is quite regular even if some fluctuation of size is still observed.

By modifying the size, shape and orientation of the milled patterns, a control over the position, number and relative orientation of MRs can be obtained. A few examples of these properties are given in Figure 5b. Rectangular patterns of $2.5\text{ }\mu\text{m} \times 1.25\text{ }\mu\text{m}$ in size (shown in the two top panels of Figure 5b) lead to 3 aligned islands with 90% probability. For $2\text{ }\mu\text{m} \times 2\text{ }\mu\text{m}$ squares instead, (shown in the two bottom panels of Figure 5b), 4 islands are obtained with a probability of 82%. It is also possible to influence the relative orientation of the resonant scatterers by simply rotating the template with respect to the silicon crystallographic axes.²⁹

Finally, statistical investigations (Figure 5c) show that, for circular patterns, small pattern scales offer the best reproducibility (top panel). Further examples obtained for $3\text{ }\mu\text{m}$ circles (top panel) fail in providing a defined multimer assembly even if a level of coordination is obtained.

These investigations highlight the versatility of this approach since the fabrication of individual or assemblies of Mie resonators were produced by tuning the dewetting speed, the silicon thickness, the pattern size and symmetry as well as the milling of local

defects acting as nucleation centers for the island growth. It is important to note that this study is focused on crystalline silicon but that amorphyticity and alloying (in particular with germanium) provide two extra degrees of freedom for the engineering of Mie resonators through spontaneous and assisted dewetting. Changes in the wettability and refractive index of the material will strongly influence both the three-dimensional shape and the optical resonances of the fabricated islands.

CONCLUSIONS

In this report, we have demonstrated that spontaneous dewetting of ultrathin SOI substrates is a flexible large-scale approach for the fabrication of subwavelength-sized Si monocrystalline nanocrystals that resonantly scatter light at visible frequencies. Correlation of far-field scattering spectroscopy to AFM imaging and full-field simulations show that these resonators reproducibly feature two radiatively damped resonances that red-shift for larger particle sizes. Our fabrication approach of dielectric scatterers is strongly versatile, as it can be applied not only to produce high-densities of MRs with high or low ordering, but also to create single monocrystalline resonators whose number and position can be tuned when the dewetting process is assisted by a LMAIS-FIB templating. This approach associates a self-assembly process (dewetting) with a top-down templating enabling the

controlled formation of complex assemblies of silicon monocrystalline resonators. This technology has a high potential in silicon photonics since it requires

only a single annealing step under an ultrahigh vacuum, and it is very effective in terms of time and cleanliness.

METHODS

Fabrication. A detailed description of the dewetting process of Si and $\text{Si}_x\text{Ge}_{1-x}$ can be found in the literature.^{29–31} The samples used for etching-assisted dewetting are processed by EBL or by LMAIS-FIB.

EBL patterns were created on SOI substrates first cleaned with organic solvents by an ultrasonic treatment. A poly(methyl methacrylate) (PMMA) layer was deposited by spinning (4000 rpm) and baked for 1 h at 160 °C after resist deposition. Scanning electron microscopy (SEM) was performed using a Philips XL30 SFESEM with a Raith Elphy Quantum lithography attachment and a Scanservice beam blanker. By reactive ion etching (RIE), about 11 nm of SOI were etched (using 50 sccm of CF_4 at a power of 50 W and a pressure of 6 mTorr).

Free patterns, such as squares and circles, were obtained by LMAIS-FIB nanomilling carried out in a Tescan LYRA1 XMH dual-beam LMAIS-FIB workstation operating at 30 keV. This LMAIS-FIB is equipped with a mass-filtered ultrahigh resolution focused ion beam COBRA-type from Orsay Physics. Patterning was performed using AuGe alloy sources and selecting a single element. In this study, most of the samples were milled with Ge^+ ions that avoid sample contamination, but Au^+ and Ga^+ were also successfully used. No remarkable differences are observed.

After *ex situ* chemical cleaning the (patterned and non-patterned) samples are immediately transferred under clean room atmosphere to the high-vacuum chamber where they are *in situ* cleaned at low temperature (600 °C for 30 min) to remove the contaminants at the Si surface. Dewetting is obtained by *in situ* ultrahigh vacuum (10^{-8} – 10^{-10} Torr) annealing at high temperatures (750–880 °C). Annealing temperature and time are adjusted depending on the dewetting stage we need (~ 25 min for partial dewetting and few hours for complete wafer dewetting) but also on the substrate thickness.

Optical Measurements. DF and BF images are obtained with a commercial LEICA DMI5000 M inverted microscope with a 100× objective lens (N.A. = 0.75). DF spectra are measured on a Olympus IX71 inverted microscope using an unpolarized 100W halogen lamp coupled to a 50× (N.A. = 0.7) reflection darkfield objective. Scattered light is collected by a 50 μm core diameter multimode fiber (that acts as a confocal pinhole) before reaching an imaging spectrometer (Acton, SP2356i) coupled to a Si-based CCD camera (Roper, Pixis-100BR-eXcelon) with a spectral resolution of about 0.6 nm (fwhm, grating 300 g/mm).

Numerical Simulations. Numerical simulations are performed by using the Finite Element Method implemented in Comsol 3.5. In a first approximation, a square faceted shape is considered with facets extension and vertical aspect ratio in agreement with the Si equilibrium shape. The in plane anisotropy which is expected to contribute at the second order is not considered. The Si resonator bearing on SiO_2/Si multilayered substrate is illuminated by a plane wave with an angle of incidence of 70 degrees and the scattered spectra is obtained for one polarization by calculating the flow of the Poynting vector over the upper half plane. The final spectra are displayed after averaging the two fundamental Transverse Electric and Transverse Magnetic polarizations. The square of the norm of the electric field is reconstructed in the vicinity of the resonator over the SiO_2 layer and Si substrate for the resonator exhibiting $L = 356$ nm and $h = 65$ nm illuminated by a plane wave with an incidence of 70°. For each polarization, the norm of the electric field averaged with that obtained with a symmetric incidence (-70°). The norm of the electric field is then averaged over the two polarizations.

Conflict of Interest: The authors declare no competing financial interest.

Acknowledgment. This work has been carried out thanks to the support of the A*MIDEX project (No. ANR-11-IDEX-0001-02) funded by the Investissements d'Avenir French Government program managed by the French National Research Agency (ANR), the French Institute Carnot Star. Work at Institut Langevin is supported by LABEX WIFI (Laboratory of Excellence within the French Program "Investments for the Future") under references ANR-10-LABX-24 and ANR-10-IDEX-0001-02 PSL*. We acknowledge M. Bollani and M. Aouassa for EBL and preliminary sample processing and investigation, G. Boudarham for preliminary numerical simulations, V. Maillard for help with darkfield spectroscopy, Fatima Bencheikh and Judikael Le Rouzo for help with reflectivity measurements, and T. David for SEM images.

Supporting Information Available: Dewetting process, dark field setup, single Mie resonators spectroscopy, spontaneous dewetting: ordered vs disordered arrays, reflectivity of macroscopic samples, E-beam assisted dewetting: MRs arrays. This material is available free of charge via the Internet at <http://pubs.acs.org/>.

REFERENCES AND NOTES

- Evlyukhin, A. B.; Reinhardt, C.; Seidel, A.; Luk'yanchuk, B. S.; Chichkov, B. N. Optical Response Features of Si-Nanoparticle Arrays. *Phys. Rev. B: Condens. Matter Mater. Phys.* **2010**, *82*, 045404.
- Evlyukhin, A. B.; Reinhardt, C.; Chichkov, B. N. Multipole Light Scattering by Nonspherical Nanoparticles in the Discrete Dipole Approximation. *Phys. Rev. B: Condens. Matter Mater. Phys.* **2011**, *84*, 235429.
- García-Etxarri, A.; Gómez-Medina, R.; Froufe-Pérez, L. S.; López, C.; Chantada, L.; Scheffold, F.; Aizpurua, J.; Nieto-Vesperinas, M.; Sáenz, J. J. Strong Magnetic Response of Submicron Silicon Particles in the Infrared. *Opt. Express* **2011**, *19*, 4815–4826.
- Evlyukhin, A. B.; Novikov, S. M.; Zywiertz, U.; Eriksen, R. L.; Reinhardt, C.; Bozhevolnyi, S. I.; Chichkov, B. N. Demonstration of Magnetic Dipole Resonances of Dielectric Nanospheres in the Visible Region. *Nano Lett.* **2012**, *12*, 3749–3755.
- Kuznetsov, A. I.; Miroshnichenko, A. E.; Fu, Y. H.; Zhang, J.; Lukyanchuk, B. Magnetic Light. *Sci. Rep.* **2012**, *2*, 492.
- Rolly, B.; Bebey, B.; Bidault, S.; Stout, B.; Bonod, N. Promoting Magnetic Dipolar Transition in Trivalent Lanthanide Ions with Lossless Mie Resonances. *Phys. Rev. B: Condens. Matter Mater. Phys.* **2012**, *85*, 245432.
- Schmidt, M. K.; Esteban, R.; Sáenz, J. J.; Suárez-Lacalle, I.; Mackowski, S.; Aizpurua, J. Dielectric Antennas—A Suitable Platform for Controlling Magnetic Dipolar Emission. *Opt. Express* **2012**, *20*, 13636–13650.
- Shi, L.; Tuzer, T. U.; Fenollosa, R.; Meseguer, F. A New Dielectric Metamaterial Building Block with a Strong Magnetic Response in the Sub-1.5-Micrometer Region: Silicon Colloid Nanocavities. *Adv. Mater.* **2012**, *24*, 5934–5938.
- Shi, L.; Harris, J. T.; Fenollosa, R.; Rodriguez, I.; Lu, X.; Korgel, B. A.; Meseguer, F. Monodisperse Silicon Nanocavities and Photonic Crystals with Magnetic Response in the Optical Region. *Nat. Commun.* **2013**, *4*, 1904.
- Albella, P.; Poyli, M. A.; Schmidt, M. K.; Maier, S. A.; Moreno, F.; Sáenz, J. J.; Aizpurua, J. Low-Loss Electric and Magnetic Field-Enhanced Spectroscopy with Subwavelength Silicon Dimers. *J. Phys. Chem. C* **2013**, *117*, 13573–13584.
- Boudarham, G.; Abdeddaim, R.; Bonod, N. Enhancing the Magnetic Field Intensity with a Dielectric Gap Antenna. *Appl. Phys. Lett.* **2014**, *104*, 021117.

12. Zywicki, U.; Evlyukhin, A. B.; Reinhardt, C.; Chichkov, B. N. Laser Printing of Silicon Nanoparticles with Resonant Optical Electric and Magnetic Responses. *Nat. Commun.* **2014**, *5*, 3402.

13. Nieto-Vesperinas, M.; Gomez-Medina, R.; Saenz, J. J. Angle-Suppressed Scattering and Optical Forces on Sub-micrometer Dielectric Particles. *J. Opt. Soc. Am. A* **2011**, *28*, 54–60.

14. Gomez-Medina, R.; Garcia-Camara, B.; Suarez-Lacalle, I.; Gonzalez, F.; Moreno, F.; Nieto-Vesperinas, M.; Saenz, J. J. Electric and Magnetic Dipolar Response of Germanium Nanospheres: Interference Effects, Scattering Anisotropy, and Optical Forces. *J. Nanophotonics* **2011**, *5*, 053512.

15. Geffrin, J. M.; Garcia-Camara, B.; Gomez-Medina, R.; Albelia, P.; Froufe-Perez, L. S.; Eyraud, C.; Litman, A.; Vaillon, R.; Gonzalez, F.; Nieto-Vesperinas, M.; *et al.* Magnetic and Electric Coherence in Forward-and Back-Scattered Electromagnetic Waves by a Single Dielectric Subwavelength Sphere. *Nat. Commun.* **2012**, *3*, 1171.

16. Person, S.; Jain, M.; Lapin, Z.; Saenz, J. J.; Wicks, G.; Novotny, L. Demonstration of Zero Optical Backscattering from Single Nanoparticles. *Nano Lett.* **2013**, *13*, 1806–1809.

17. Fu, Y. H.; Kuznetsov, A. I.; Miroshnichenko, A. E.; Yu, Y. F.; Lukyanchuk, B. Directional Visible Light Scattering by Silicon Nanoparticles. *Nat. Commun.* **2013**, *4*, 1527.

18. Staude, I.; Miroshnichenko, A. E.; Decker, M.; Fofang, N. T.; Liu, S.; Gonzales, E.; Dominguez, J.; Luk, T. S.; Neshev, D. N.; Brener, I.; *et al.* Tailoring Directional Scattering through Magnetic and Electric Resonances in Subwavelength Silicon Nanodisks. *ACS Nano* **2013**, *7*, 7824–7832.

19. Spinelli, P.; Verschueren, M.; Polman, A. Broadband Omnidirectional Antireflection Coating Based on Subwavelength Surface Mie Resonators. *Nat. Commun.* **2012**, *3*, 692.

20. Rolly, B.; Stout, B.; Bonod, N. Boosting the Directivity of Optical Antennas with Magnetic and Electric Dipolar Resonant Particles. *Opt. Express* **2012**, *20*, 20376–20386.

21. Rolly, B.; Geffrin, J.-M.; Abdeddaim, R.; Stout, B.; Bonod, N. Controllable Emission of a Dipolar Source Coupled with a Magneto-Dielectric Resonant Subwavelength Scatterer. *Sci. Rep.* **2013**, *3*, 3063.

22. Bezares, F. J.; Long, J. P.; Glembotck, O. J.; Guo, J.; Rendell, R. W.; Kasica, R.; Shirey, L.; Owrutsky, J. C.; Caldwell, J. D. Mie Resonance-Enhanced Light Absorption in Periodic Silicon Nanopillar Arrays. *Opt. Express* **2013**, *21*, 27587–27601.

23. Krasnok, A. E.; Filonov, D. S.; Simovski, C. R.; Kivshar, Y. S.; Belov, P. A. Experimental Demonstration of Superdirective Dielectric Antenna. *Appl. Phys. Lett.* **2014**, *104*, 133502.

24. Evlyukhin, A. B.; Eriksen, R. L.; Cheng, W.; Beermann, J.; Reinhardt, C.; Petrov, A.; Prorok, S.; Eich, M.; Chichkov, B. N.; Bozhevolnyi, S. I. Optical Spectroscopy of Single Si Nanocylinders with Magnetic and Electric Resonances. *Sci. Rep.* **2014**, *4*, 4126.

25. Sutter, P.; Ernst, W.; Choi, Y.; Sutter, E. Mechanisms of Thermally Induced Dewetting of Ultrathin Silicon-on-Insulator. *Appl. Phys. Lett.* **2006**, *88*, 141924–141924.

26. Pierre-Louis, O.; Chame, A.; Saito, Y. Dewetting of Ultrathin Solid Films. *Phys. Rev. Lett.* **2009**, *103*, 195501.

27. Zhang, P.; Yang, B.; Rugheimer, P.; Roberts, M.; Savage, D.; Liu, F.; Lagally, M. Influence of Germanium on Thermal Dewetting and Agglomeration of the Silicon Template Layer in Thin Silicon-on-Insulator. *J. Phys. D: Appl. Phys.* **2009**, *42*, 175309.

28. Dufay, M.; Pierre-Louis, O. Anisotropy and Coarsening in the Instability of Solid Dewetting Fronts. *Phys. Rev. Lett.* **2011**, *106*, 105506.

29. Aouassa, M.; Favre, L.; Ronda, A.; Maaref, H.; Berbezier, I. The Kinetics of Dewetting Ultra-Thin Si Layers from Silicon Dioxide. *New J. Phys.* **2012**, *14*, 063038.

30. Aouassa, M.; Berbezier, I.; Favre, L.; Ronda, A.; Bollani, M.; Sordan, R.; Delobbe, A.; Sudraud, P. Design of Free Patterns of Nanocrystals with *ad hoc* Features via Templated Dewetting. *Appl. Phys. Lett.* **2012**, *101*, 013117–013117.

31. Berbezier, I.; Aouassa, M.; Ronda, A.; Favre, L.; Bollani, M.; Sordan, R.; Delobbe, A.; Sudraud, P. Ordered Arrays of Si and Ge Nanocrystals via Dewetting of Pre-Patterned Thin Films. *J. Appl. Phys.* **2013**, *113*, 064908–064908.

32. Becker, J.; Grün, G.; Seemann, R.; Mantz, H.; Jacobs, K.; Mecke, K. R.; Blossey, R. Complex Dewetting Scenarios Captured by Thin-Film Models. *Nat. Mater.* **2003**, *2*, 59–63.

33. Quéré, D. Wetting and Roughness. *Annu. Rev. Mater. Res.* **2008**, *38*, 71–99.

34. Fowlkes, J. D.; Kondic, L.; Diez, J.; Wu, Y.; Rack, P. D. Self-Assembly *versus* Directed Assembly of Nanoparticles via Pulsed Laser Induced Dewetting of Patterned Metal Films. *Nano Lett.* **2011**, *11*, 2478–2485.

35. Ye, J.; Thompson, C. V. Templated Solid-State Dewetting to Controllably Produce Complex Patterns. *Adv. Mater.* **2011**, *23*, 1567–1571.

36. Ishikawa, Y.; Kumezawa, M.; Nuryadi, R.; Tabe, M. Effect of Patterning on Thermal Agglomeration of Ultrathin Silicon-on-Insulator Layer. *Appl. Surf. Sci.* **2002**, *190*, 11–15.

37. Cheynis, F.; Bussmann, E.; Leroy, F.; Passanante, T.; Müller, P. Dewetting Dynamics of Silicon-on-Insulator Thin Films. *Phys. Rev. B: Condens. Matter Mater. Phys.* **2011**, *84*, 245439.

38. Bussmann, E.; Cheynis, F.; Leroy, F.; Müller, P.; Pierre-Louis, O. Dynamics of Solid Thin-Film Dewetting in the Silicon-on-Insulator System. *New J. Phys.* **2011**, *13*, 043017.

39. Mertens, H.; Koenderink, A. F.; Polman, A. Plasmon-Enhanced Luminescence Near Noble-Metal Nanospheres: Comparison of Exact Theory and an Improved Gersten and Nitzan Model. *Phys. Rev. B: Condens. Matter Mater. Phys.* **2007**, *76*, 115123.

40. van de Groep, J.; Polman, A. Designing Dielectric Resonators on Substrates: Combining Magnetic and Electric Resonances. *Opt. Express* **2013**, *21*, 26285–26302.

41. Leroy, F.; Cheynis, F.; Passanante, T.; Müller, P. Dynamics, Anisotropy, and Stability of Silicon-on-Insulator Dewetting Fronts. *Phys. Rev. B: Condens. Matter Mater. Phys.* **2012**, *85*, 195414.

42. Sapienza, L.; Thyrrestrup, H.; Stobbe, S.; Garcia, P. D.; Smolka, S.; Lodahl, P. Cavity Quantum Electrodynamics with Anderson-Localized Modes. *Science* **2010**, *327*, 1352–1355.

43. Vynck, K.; Burresi, M.; Riboli, F.; Wiersma, D. S. Photon Management in Two-Dimensional Disordered Media. *Nat. Mater.* **2012**, *11*, 1017–1022.

44. Strudley, T.; Zehender, T.; Blejean, C.; Bakkers, E. P.; Muskens, O. L. Mesoscopic Light Transport by Very Strong Collective Multiple Scattering in Nanowire Mats. *Nat. Photonics* **2013**, *7*, 413–418.

45. Wiersma, D. S. Disordered Photonics. *Nat. Photonics* **2013**, *7*, 188–196.

46. Riboli, F.; Caselli, N.; Vignolini, S.; Intonti, F.; Vynck, K.; Barthelemy, P.; Gerardino, A.; Balet, L.; Li, L. H.; Fiore, A.; *et al.* Engineering of Light Confinement in Strongly Scattering Disordered Media. *Nat. Mater.* **2014**, *13*, 720–725.

47. Wu, C.; Arju, N.; Kelp, G.; Fan, J. A.; Dominguez, J.; Gonzales, E.; Tutuc, E.; Brener, I.; Shvets, G. Spectrally Selective Chiral Silicon Metasurfaces Based on Infrared Fano Resonances. *Nat. Commun.* **2014**, *5*, 3892.

48. Chong, K. E.; Hopkins, B.; Staude, I.; Miroshnichenko, A. E.; Dominguez, J.; Decker, M.; Neshev, D. N.; Brener, I.; Kivshar, Y. S. Observation of Fano Resonances in All-Dielectric Nanoparticle Oligomers. *Small* **2014**, *10*, 1985–1990.